Journal of Alloys and Compounds 969 (2023) 172375

Contents lists available at ScienceDirect

Journal of Alloys and Compounds

journal homepage: www.elsevier.com/locate/jalcom

Revealing direct atomic structure and electrostatic maps of the Ruddlesden-Popper faults in $LaNiO_3$ perovskite

Yuanmin Zhu [a,*], Ping Liao [a], Wandong Xing [b,*], Jiayu Liu [a], Jizhe Cui [c], Cai Jin [d], Lang Chen [d], Biao Wang [a,*], Rong Yu [c]

[a] Research Institute of Interdisciplinary Science & School of Materials Science and Engineering, Dongguan University of Technology, Dongguan 523808, China
[b] State Key Laboratory of Photocatalysis on Energy and Environment, College of Chemistry, Fuzhou University, Fuzhou 350002, China
[c] National Center for Electron Microscopy in Beijing, School of Materials Science and Engineering, Tsinghua University, Beijing 100084, China
[d] Department of Physics, Southern University of Science and Technology, Shenzhen 518055, China

ARTICLE INFO

Keywords:
$LaNiO_3$ films
Ruddlesden-Popper faults
Atomic structure imaging
DFT calculations

ABSTRACT

Ruddlesden-Popper (RP) faults in perovskites as one type of the anti-phase boundaries provide a versatile platform to manipulate the magnetic, conducting, and magnetoresistance properties in the complex oxides. Local fine structure at the boundaries containing light atoms is a key factor to understand the underlying structure-function relationship due to their interfaces mediated effects. In this work, the atomic structure, chemical distribution and electronic structure of typical RP faults in perovskite $LaNiO_3$ and its epitaxial nanocomposite films on a $SrTiO_3$ substrate were systematically investigated combining high-resolution scanning transmission electron microscopy (STEM) and density functional theory (DFT) calculations. Integrated differential phase contrast (iDPC) STEM imaging results demonstrate a NiO_{2-x}-(LaO-LaO)-NiO_{2-x} atomic configuration with content fluctuations of oxygen at the RP faults. Atomic electronic energy loss spectroscopy results and DFT calculations illustrate that Ni cations have mixed valence of Ni^{2+}, Ni^{3+} at the RP faults accompanying with oxygen environment fluctuations affected by the non-stoichiometric bonding. This study offers a comprehensive route to explore intriguing chemical structures and physical properties in the homointerface structure at the atomic level.

1. Introduction

Heterostructures with abundant combination forms open new opportunities for the design of next-generation electronic devices due to their enthralling interface-mediated effects, in which the interfaces provide a versatile platform to control the interplay of the order-parameters (i.e. lattice, orbital, charge, and spin) in functional oxides [1–5]. In particular, there are also interface structures existing in one single-crystal phase, called antiphase boundaries (APBs) or domain structures, which also have a strong influence on the magnetic, conducting, electrochemical, and magneto-resistance properties of these functional materials [6–11].

APBs are often present in epitaxially thin films, which are grown in a layer-by-layer mode or two-dimensional islands growth mode [6]. For describing the APBs, some possible independent shift vectors, *R*, can be indexed as the fractional [0,0,0]- (no shift), [110]-, [$\bar{1}\bar{1}$0]-, [100]- and [101]-directions. Among the diverse APBs, there is one type of APB, often referred to as Ruddlesden-Popper (RP) faults, which is frequently reported in perovskite epitaxial thin films [12–15]. Recently, benefiting from the high-angle annular dark-field scanning transmission electron microscopy technology (HAADF-STEM), atomic models have been proposed to describe the geometry and formation mechanism of RP faults in various perovskite film systems, for example, $Sr_{n+1}Ti_nO_{3n-1}$ [12], $LaNiO_3$ [16], $La_2SrMn_3O_{10}$ [17], (Sr,Ca)TiO_3 [18], and La_2NiO_4 [19]. The two perfect ideal perovskite ABO_3 blocks normally have a $a/2$[111] displacement vector across a RP fault while displaying a $a/2$[110] in-plane translational vectors in [100] projections. The RP faults in perovskite materials can critically affect the electronic, magnetic properties of these complex oxides, promote cation diffusions through the defects path, or even induce exciting new physical properties just at the APB structures. Exploring more details about the atomic structure electronic structure and related charge states in the APB structures is fundamental in understanding their physicochemical essences in the perovskite films as well as the heteroepitaxial composite film systems.

$LaNiO_3$ is a perovskite structure with a rhombohedral distortion (S.G. *R3c* 161) [20]. It has a lattice parameter of a_{pc}= 3.83 Å, while the

* Corresponding authors.
E-mail addresses: zhuyuanm@dgut.edu.cn (Y. Zhu), xwd@fzu.edu.cn (W. Xing), wangbiao@mail.sysu.edu.cn (B. Wang).

https://doi.org/10.1016/j.jallcom.2023.172375
Received 22 March 2023; Received in revised form 26 September 2023; Accepted 30 September 2023
Available online 2 October 2023

subscript *pc* represents the pseudo-cubic perovskite lattice. $LaNiO_3$ has drawn a considerable spotlight because of its exceptional transport properties at room temperature and potential tunability of electrical-magnetic coupling through epitaxial strain engineering [21]. A metal to insulator transition can be induced in the $LaNiO_{3-x}$ compound by oxygen concentration regulation. Standard $LaNiO_3$ has trivalent Ni^{3+}, is a n-type metallic oxide, exhibiting a Pauli paramagnetism. The oxygen-deficit $LaNiO_{2.5}$ has divalent Ni^{2+}, is an insulator and is antiferromagnetic with a T_N temperature at 320 K. Between the above phases, $LaNiO_{2.75}$ has a mixed valence (Ni^{3+}/Ni^{2+}) and displays a subtle metal to insulator transition at about 75 K [22]. In our previous study, a $LaNiO_3$-NiO heteroepitaxial oxide film was investigated as the model material system, and the atomic structure of its heterointerface is demonstrated to be $(La\text{-}O/La\text{-}O)_{LaNiO3}/(Ni\text{-}O)_{NiO}$ [23]. However, the detailed APBs structure only in the $LaNiO_3$ matrix phase has yet to be investigated, which is a prerequisite to understand the variations of chemical distribution and electronic properties in the nanocomposite heterostructures.

Driven by the above thoughts, in this work, we systematically investigated the fine structure of RP faults both in the pure $LaNiO_3$ film and in the $LaNiO_3$ matrix phase of the $LaNiO_3$-NiO heterostructures grown on a (001)-oriented $SrTiO_3$ substrate. Combining aberration-corrected high-angle angular dark-field (HAADF) with differential phase contrast (DPC) STEM imaging technologies and density functional theory (DFT) calculations, the atomic arrangement including the oxygen atom and electronic structures at the RP faults in the epitaxial film systems was investigated systematically at an atomic level.

2. Experimental

2.1. Thin-film growth

The vertically aligned heteroepitaxial nanocomposite films of $LaNiO_3$-NiO were deposited on the (001)-$SrTiO_3$ substrates by pulsed laser deposition. The growth conditions were a temperature of 800 ℃ and an oxygen atmosphere of 100 mTorr, and laser frequency of 10 Hz. Similarly, the pure $LaNiO_3$ films were grown at 700 ℃ under an oxygen pressure of 100 mTorr using a laser frequency of 10 Hz. In particular, the $LaNiO_3$-NiO heteroepitaxial films were deposited using a computer-controlled targets system with two separated $LaNiO_3$ and NiO targets. Therefore, the volume fraction of $LaNiO_3$ and NiO can be archived by controlling the number of laser pulses hitting on each oxide target based on the deposition rates of $LaNiO_3$ and NiO films. In this work, the volume fraction of deposited $LaNiO_3$-NiO composited films is about 7:3 (laser pulses number: $LaNiO_3$-NiO=70:30).

2.2. TEM characterizations

Plan-view and cross-section TEM samples for transmission electron microscopy (TEM) and STEM studies were prepared by standard steps. Firstly, the samples were mechanical grinded to the thickness of samples to 20 μm. Secondly, the grounded samples were fine-milled to thin enough for the TEM observation by an ion milling equipment (Leica EM RES 102). Before mechanical grinding, the cross-sectional sample was glued together face-to-face (film) with silicon slices like a sandwich. A thin TEM sample of the $LaNiO_3$ film with a 30-nm thickness was prepared for the iDPC-STEM experiments by a 2-dimensional transfer method introduced by our previous publication [24]. The iDPC-STEM image simulations were performed by the typical multislice method with microscope parameters of Cs= 150 nm, Defocus= 6 nm, Thickness= 30 nm. Morphology, atomic structural and chemical investigations were carried out by using a TITAN Themis 60–300 microscope (Thermo Fisher Scientific Ltd.) with the information limit of 0.6 Å, equipped with double Cs correctors and Super energy dispersion X-ray detector. The probe convergence angle is 25 mrad and the detection angles used for HAADF-, iDPC-STEM imaging were 64–200 and 6–22 mrad, respectively. The atomic EDS data were acquired at the beam current of 120 pA for ~8 min. The dual-EELS technology is used to collect zero-loss and high-loss edges simultaneously on a Gatan Quantum 965 spectrometer. And a 0.0005 s and 0.5 s exposure time were used for each zero-loss and high-loss edge spectrum, respectively. The high-loss edges are post-analyzed in the Digital Micrograph software. The zero-loss and high-loss edges are firstly aligned simultaneously before analyzing the chemical shift. For clarity, a slight smoothing was applied to the Ni *L* edges and no other normalization, summation methods of all the EELS data are performed.

2.3. DFT calculations

The DFT calculations were carried out using the Project-Augmented Wave (PAW) method through the Vienna Ab-initio Simulation Package (VASP) code [25,26]. Considering the strong Coulomb interactions between the electrons in Ni-3*d* orbit, the calculations were performed using the GGA+*U* approximation approach with the Perdew-Burke-Ernzerhof (PBE) scheme. Following previous studies [27–29], we adopted Hubbard U corrections with U = 5.3 eV for Ni. The kinetic energy cut-off for the plane-wave expansion was set to 500 eV. The k-points were generated using the Monkhorst-Pack mesh [30]. For La, Ni, and O, 5 $s^2 5p^6 5d^1 6\ s^2$, $3d^8 3\ s^2$, and $2\ s^2 2p^4$ orbitals were taken as valence states, respectively. For the bulk $LaNiO_3$, the rhombohedral cell was first relaxed to obtain the lattice parameter, i.e., a= 5.384 Å and the rhombohedral angle 60.83°. For the APB structures, the unrelaxed unit cell was 5.452 Å × 5.452 Å × 43.332 Å and both the upper and lower interfaces contained six LaO layers and six NiO_2 layers. Subsequently, the relaxations of the atomic positions and lattice parameters were performed with a 7 × 7 × 1 k-point grid. And the division was increased to 15 × 15 × 1 for calculating the density of states (DOS). The convergence criterion was 0.01 eV/Å for structural relaxations. For the bond valence sum (BVS) analysis in our work [31], we employed the KDist package equipped in the Kalvados software.

3. Results and discussion

The typical low-magnification morphology of the RP faults from the $[001]_{pc}$ direction (plan-view) in the epitaxial pure $LaNiO_3$ film on a (001) oriented $SrTiO_3$ substrate are given in Fig. S1. A mass of RP faults (strip lines) was observed in the $LaNiO_3$ phase with 90-degree biaxial distributions. Similar morphology of the RP faults was also observed in the $LaNiO_3$-NiO heteroepitaxial films (Fig. S2), which will be discussed together in the following part.

To observe the atomic structure of the RP faults, high resolution HAADF-STEM images of the APB structures in the $LaNiO_3$ phase as well as in the $LaNiO_3$-NiO heterostructures were investigated from plan-view direction, as shown in Fig. 1. With the NiO phase embedded in the $LaNiO_3$ matrix, we want to investigate the in-plane strain effects on the origin and behaviors of the RP faults. Considering the effect of atomic numbers, HAADF-STEM imaging is a favorable technology to display the chemical composition variations in composite structures due to its Z-dependent contrast. In $LaNiO_3$ phase, the atomic contrast of La columns is much brighter than that of the Ni columns in Fig. 1. Obviously, 90-degree bending APBs were observed in the pure $LaNiO_3$ films as indicated by the red dotted lines in Fig. 1a. The atomic arrangements of the APBs structure along $[001]_{pc}$ direction observed in Fig. 1a can be concluded to be NiO_2-(LaO-LaO)-NiO_2, where the two LaO layers are stacked together with a shift vector of $1/2a[110]_{pc}$ or $1/2a[\bar{1}10]_{pc}$. This RP fault in LNO is actually a type of stacking faults and the lattice displacement at the RP faults can induce an abrupt shear strain (e_{xy}) in the HRSTEM images, which can be displayed easily by Geometric Phase Analysis (GPA) method. Here, the strain e_{xy} map of Fig. 1a is performed by GPA tool and given in Fig. 1b, showing a strong lattice distortion contrast at the RP faults correspondingly to the HRSTEM image (Fig. 1a). The (100) and

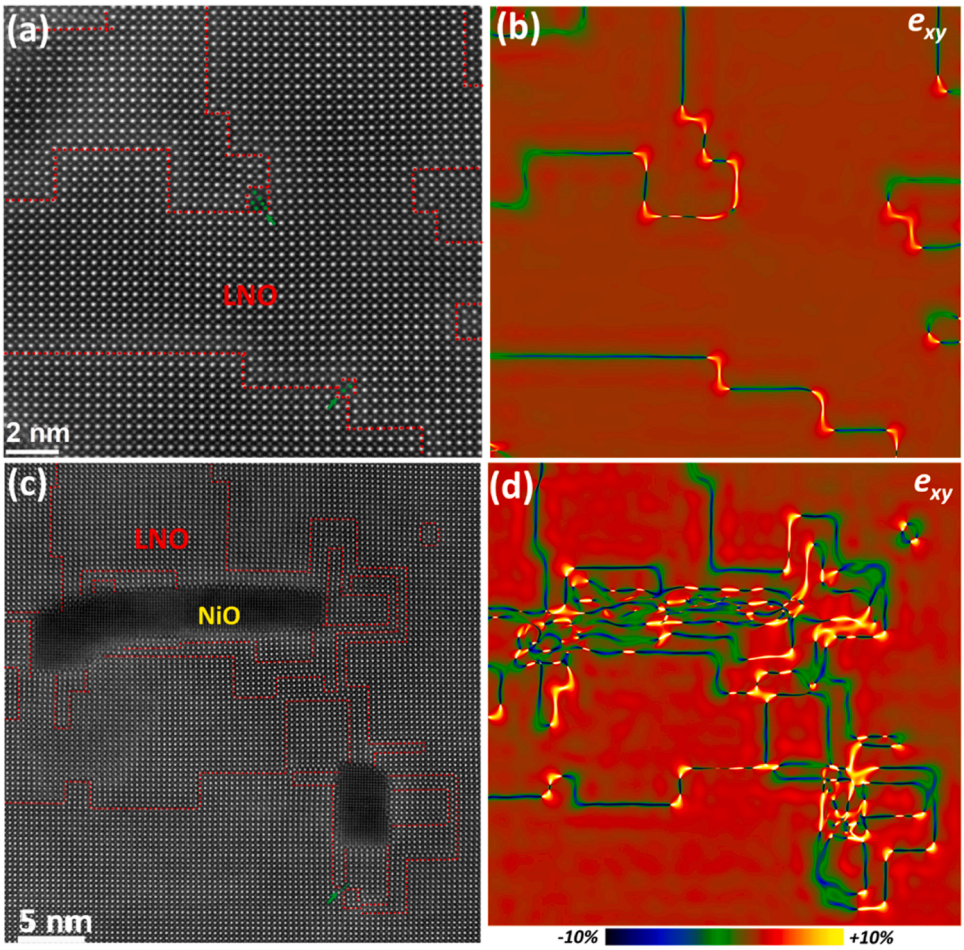

Fig. 1. (a) High-resolution HAADF-STEM image of the RP faults in pure $LaNiO_3$ film from the $[001]_{pc}$ direction. (b) The GPA strain map (e_{xy}) of the HAADF-STEM image (a) along the $LaNiO_3$ RP faults, performed by GPA tool using $(100)_{pc}$ and $(010)_{pc}$ diffraction spots. (c) A HAADF-STEM image of the RP faults in $LaNiO_3$ matrix phase observed in the $LaNiO_3$-NiO heterostructures along $[001]_{pc}$ crystal direction. (d) The misfit strain map (e_{xy}) of the image (c), correspondingly.

(010) diffraction spots are selected as *x, y* vectors and the strain maps of e_{xx}, e_{yy} are shown in the Fig. S3, displaying the RP faults along [100], [010] directions. Furthermore, high-density RP faults in $LaNiO_3$ phase were also observed in the $LaNiO_3$-NiO heterostructures, shown in Fig. 1c. The corresponding misfit strain map (e_{xy}) of Fig. 1c is given in Fig. 1d, respectively, displaying an obvious one-to-one contrast of RP faults. Interestingly, these RP faults often originated at the $LaNiO_3$-NiO heterointerfaces, which means that the lattice misfit strain is a dominant factor in its formation. The contrast of the e_{xy} maps in Fig. 1b and d illustrated that the shear strains along the [110] direction are mostly compressive at the center area of the RP faults, but it becomes tensile at the corner area. This is possibly attributed to the greater lattice distortions at the corners of the RP faults. The green dots in Fig. 1a and c overlapped on the Ni atoms indicate that the Ni-O*x* atomic aggregations occur at the corner of the RP faults. According to the $LaNiO_3$-NiO composited heterostructures, we can infer that the Ni-O*x* aggregations mostly are nanosized NiO phase in the $LaNiO_3$ film when the La-rich RP faults form. Because the O atom does not show contrasts in HAADF images, it hinders further understanding the real chemical information of the fault structures. More atomic information, especially the O-atom position, needs to be investigated carefully in the APBs areas.

The HAADF imaging technology combined energy-dispersive X-ray spectra (EDS) provides a powerful route to investigate both atomic structural and chemical information in real space. Fig. 2 shows the atomic-scale EDS maps on a localized RP fault. The typical RP fault was imaged along [001] direction (Fig. 2a). Chemical maps are shown for the La *L* edge (Fig. 2b), the Ni *K* edge (Fig. 2c), and the composite of the La and Ni maps (Fig. 2d). The chemical maps are slightly filtered by a Gauss filter. Therefore, it is found to be a one-to-one correspondence between the HAADF image and the elemental EDS maps at atomic level, which gives a direct interpretation of the RP faults structures. Two LaO layers were directly connected at the RP fault boundaries, showing in Fig. 2b.

To reveal the atomic structure and electronic structure of the RP faults, detailed DPC-STEM investigations containing integrated differential phase contrast (iDPC) and (differentiated differential phase contrast) dDPC techniques were performed and the results are shown in Fig. 3. The iDPC-STEM technique is demonstrated to have capability for imaging both light and heavy elements with near-linear contrast to the Z number in the sample [32]. The dDPC-STEM technique can be applied to directly visualize the electric field and charge of atoms and to reveal local chemical bonding states within crystals. Fig. 3a gives a typical iDPC-STEM image showing obvious RP fault boundaries, in which both La, Ni, and O atoms can be observed with linear contrast. The sample thickness for the DPC-STEM investigations is about 30-nm thickness using a specific method introduced by our previous publication [24], which can help remove thickness effects on the image contrast. Image simulations for the iDPC image of the RP faults structure using the multislice method also confirm that the sample thickness is close to 30 nm (Fig. S4). Thus, we can quantitatively analyze the relationship between contrast of atomic columns and their content change. The La, Ni, O atoms can be distinguished and marked as brown, green and red dots on the columns, respectively. It can be deduced that the chemical bonding layers at the RP faults are NiO_2-(LaO-LaO)-NiO_2 from the iDPC-STEM image contrast. The intensity fluctuations of the O atoms

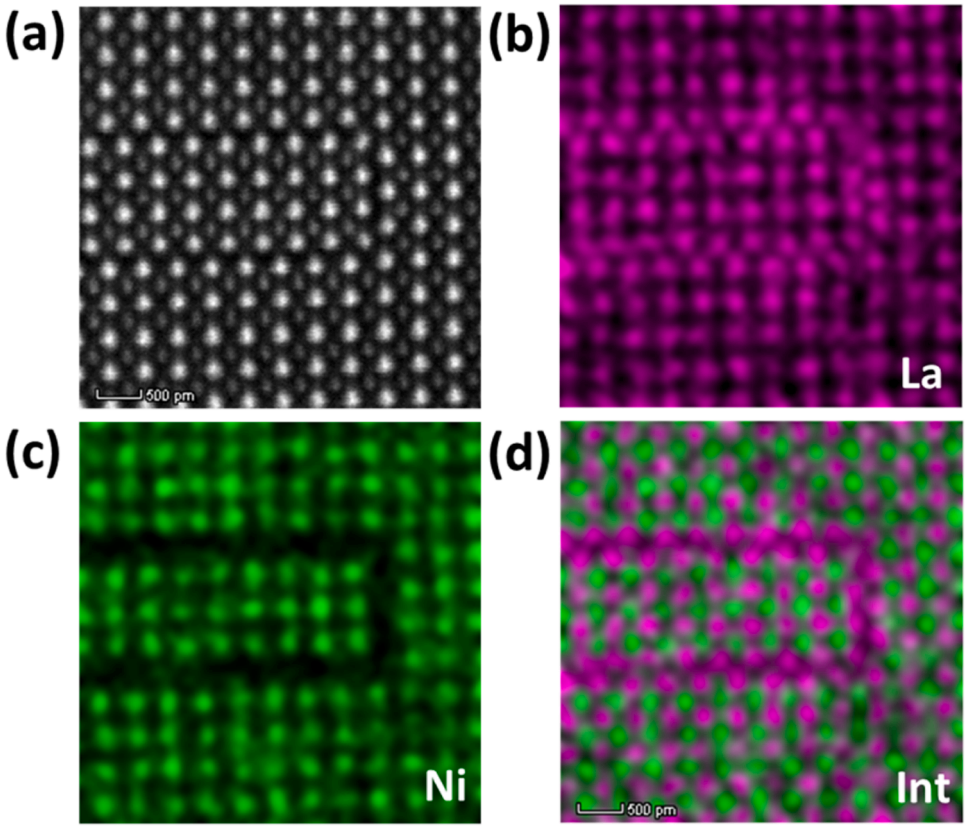

Fig. 2. Atomic EDS investigation of the $LaNiO_3$ RP faults. (a) HAADF-STEM image. The corresponding atomic EDS maps: (b)La map, (c)Ni map, and (d) the integrated map of La and Ni.

near and far away from the RP faults were investigated systematically in Fig. 3a along the red and green dashed arrows, respectively. The corresponding results are shown in Fig. 3b and c. It is found that the atomic intensity of O columns in the nearest NiO_2 layers at the RP faults is lower than that in the off-interface NiO_2 and La-O layers (Fig. 3b). On the contrary, the linescan of O columns from the bulk area along the green dashed arrow shows an almost similar intensity both in the NiO_2 and LaO layers (Fig. 3c). It demonstrates that there are some content fluctuations of the oxygen columns in the nearest NiO_2 and LaO layers at the RP faults, especially in the NiO_2 layers. To investigate the electrostatic structure of the RP faults, DPC-STEM and dDPC-STEM imaging and processing are performed at the same area. The DPC-STEM and dDPC-STEM images are derived from the four segmented-detector images (Fig. S5) using the introduced method [33–35]. The color and intensity of electric field vector map correspond to the relative direction and strength of electric field at each atom in the DPC-STEM image (Fig. 3d), illustrating the local uneven distribution of the electric field at the LaO layer in the RP faults (white arrows). The dDPC-STEM constructs an image that its contrast is proportional to the total charge density at each position. Fig. 3e gives the calculated corresponding dDPC-STEM images showing the atomic total charge density map. The total charge density is normalized by the number of unit cells along the beam direction based on the sample thickness. An integrated intensity profile of the charge density at the RP faults along the red arrow is given in Fig. 3f. It is demonstrated that the total charge density is decreased in the nearest NiO_2 and LaO layers at the RP faults. Therefore, fluctuations of the oxygen content and electrostatic structure variations in the RP faults are believed to be highly related to the electrical charge imbalance problem.

The precise atomic structure of the RP faults in $LaNiO_3$, observed in the above iDPC-STEM images, can be written as NiO_{2-x}-(LaO_y-LaO_y)-NiO_{2-x}, with content fluctuations of oxygen and charge density variations at the interface layers. What are the effects of the oxygen fluctuations in the interfacial NiO_2 and LaO layers on the electronic structure and chemical environment of the RP fault structure is a key problem to study. This will be investigated further through the atomic electron energy loss spectroscopy (EELS).

Fig. 4 gives a dual-EELS line scan investigation which is obtained simultaneously for the Ni *L*, O *K* and zero-loss edges along the atomic RP fault structure. Series of EELS spectrums from number 1–8 are shown in Fig. 4b, extracted from the line scan dataset marked as the yellow dotted line in Fig. 4a. Among them, the 4th and 5th profiles are extracted exactly from the two adjacent Ni columns in the vicinity of the RP fault. It is well known that one metal at a higher oxidation state often has a larger electron energy loss or binding energy at its $L_{2,3}$ edge than that in its lower oxidation state in the EELS or XPS fields. In Fig. 4b-c, there shows a detectable chemical shift of Ni $L_{2,3}$ edges between the Ni ion columns near the RP faults (4th and 5th) and the others in bulk $LaNiO_3$ phase. Exactly, the enlarged Ni L_3 edges given in Fig. 4c illustrates a chemical shift of about 0.4 eV calculated by the positions of peak maximum. It indicated a lower valence state of the Ni ions at the RP faults, which can be attributed to oxygen deficiencies [36].

The O *K* edges along the APB interface were also collected as corresponding EELS line scans with the Ni *L* edges shown in Fig. 4d. The corresponding low loss EELS linscan dataset of the O *K* edge was shown in Fig. S6. There are three main peaks at 532 eV, 537 eV, and 545 eV in the O *K* edges. Noticeably, the peaks at 532 eV become blunt for the 4th and 5th spectrums compared with other spectrums, as is observed by the red arrows, which illustrate an increase in oxygen vacancies around the Ni cations at the RP faults interface. It has obvious variations, responsing to the chemical shifts of Ni ions. Above all, the EELS linescanes results demonstrate that the Ni cation at the RP faults has a mixed valence of Ni^{2+}, Ni^{3+}, which is attributed to the non-stoichiometric chemical bonding (i.e., NiO_{2-x}-(LaO_y-LaO_y)-NiO_{2-x}) in the APBs. Further evidence

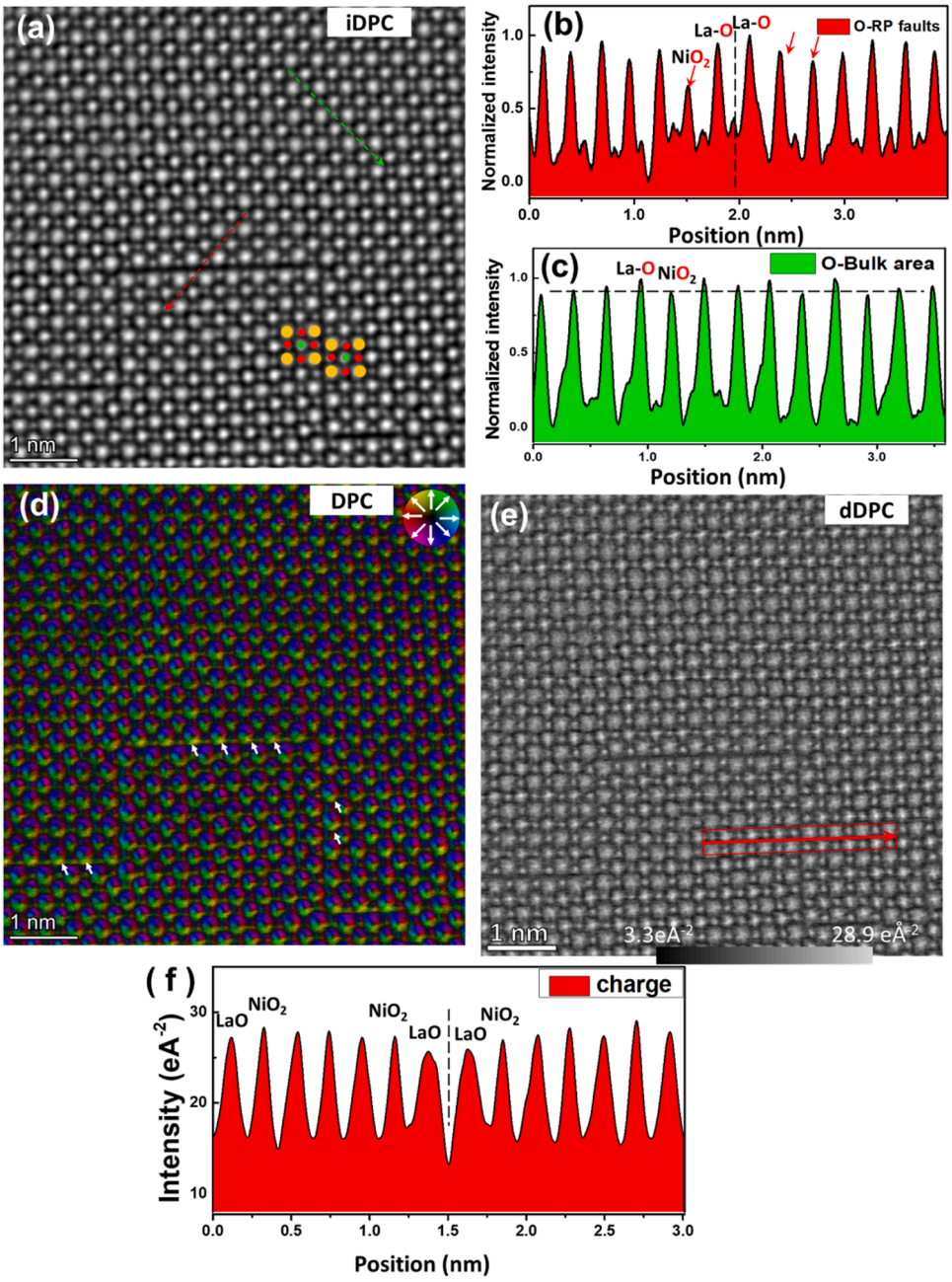

Fig. 3. (a) Atomic iDPC-STEM image of RP faults in $LaNiO_3$ film along $[001]_{pc}$ axis. The brown, green and red dots marked on the atomic columns represent La, Ni, O atoms respectively. (b) Line profile of the O contrast along the RP fault from (a) (red dashed arrow). (c) Line profile (green dashed arrow) of the O contrast in the pure perovskite area from (a). Corresponding electric field vector, strength map (d) and total charge map (e) of RP faults in $LaNiO_3$ along the [001] zone axis in (a) derived from the four segmented-detector images. The total charge density in (c) is normalized by the number of unit cells. (f) Total charge intensity profile of the LaO layer and NiO_2 layers across the RP faults subtracted from the red arrow in (e).

can be found in the supplementary materials that a short ordered RP phase was observed displaying the atomic arrangements of a $[001]_{pc}$ La_2NiO_4 structure with Ni^{2+} ions (Fig. S7). Our observation of the mixed valence of Ni^{2+}, Ni^{3+} existing in RP faults is helpful to understand related physical properties such as electrical transportation in this material system. It should be noted that there are some minor variations observed in the series of the O *K* spectra. One is that the tail region of the O K edges around the 545 eV, and 570 eV are decreased slightly from spectra 1–8, which is believed to be related to the carbon contamination at the latter half of the line scan area (light white contrast in the lower part of Fig. 4a). Another is that a gradual peak shift was observed the series spectra from 1st to 8th, which may be affected by the sample conditions or the complex interactions of oxygen and other impurity elements. However, these minor variations can't cover up the changes in the peak shape at 532 eV between the RP faults interface and bulk area. Therefore, in our opinion, the main conclusion of mixed valence of Ni ions existing at the RP faults both observed in the Ni *L* and O *K* spectra is not affected.

To reveal the nature of the RP faults, we constructed atomic models of the APB interface by means of the obtained STEM images and performed DFT+U calculations. However, we were unable to obtain the exact content fluctuations of oxygen atoms in the nearest LaO and NiO_2 layers at the RP faults. In order to simplify the calculation, we considered four configurations with and without oxygen vacancies (V_O) in the nearest NiO_2 and LaO layers: NiO_2-(LaO-LaO)-NiO_2 (Fig. S8a), NiO_2-($LaO_{0.5}$-$LaO_{0.5}$)-NiO_2 (Fig. S8b), $NiO_{1.5}$-(LaO-LaO)-$NiO_{1.5}$ (Fig. 5a), and

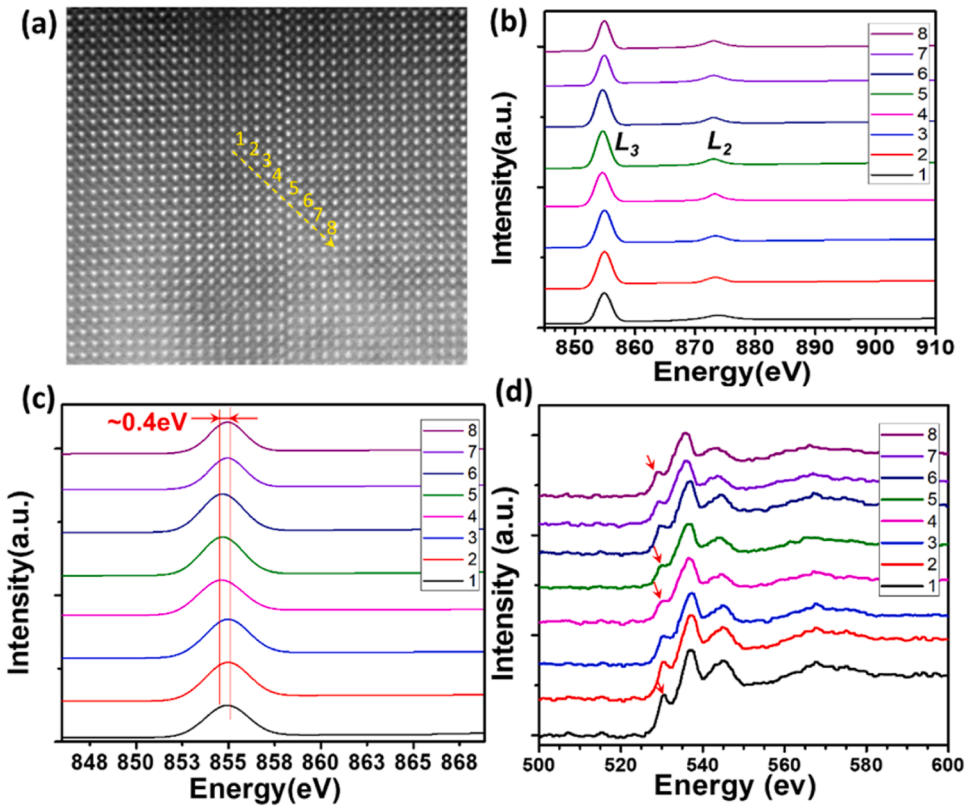

Fig. 4. (a) A high-resolution HAADF-STEM image of a RP fault in $LaNiO_3$ phase. (b) Series of EELS line scans of Ni $L_{2,3}$ edge along the RP fault extracted from the yellow dotted arrow in (a). (c) The enlarged Ni L_3 edge displaying a chemical shift of about 0.4 eV at the RP faults. (d) Extracted atomic EELS line scans of O *K* edges along the RP faults.

$NiO_{1.5}$-($LaO_{1.5}$-$LaO_{1.5}$)-$NiO_{1.5}$ (Fig. S8c). Noticeably, as shown in Fig. S8b, the NiO_2-($LaO_{0.5}$-$LaO_{0.5}$)-NiO_2 model is not consistent well with our iDPC-STEM observations, which indicates that the V_O could not be formed in the LaO layers. In addition, the optimized $NiO_{1.5}$-($LaO_{1.5}$-$LaO_{1.5}$)-$NiO_{1.5}$ model is similar to the NiO_2-(LaO-LaO)-NiO_2 model. The CIF structure file of NiO1.5-(LaO-LaO)-NiO1.5 is provided in supplementary material. To estimate approximately the oxidation state of each atom in the APB models, we calculated the BVS values of the La and Ni ions near the interface. As shown in Fig. 5b, for the $NiO_{1.5}$-(LaO-LaO)-$NiO_{1.5}$ model, the BVS values of Ni atoms especially at the $NiO_{1.5}$ layer decrease to ~2.36, illustrating a nominal oxidation state of 2+. The decreased oxidation state is consistent with the EELS results. However, for the ideal NiO_2-(LaO-LaO)-NiO_2 model, the Ni atoms at the NiO_2 layer have a nominal oxidation state of 3+, which is inconsistent with the EELS results.

To indicate the relative stability between $LaNiO_3$-APB and $LaNiO_3$, the formation energy is calculated. The following definition: $E_f = [E(La_mNi_nO_l) - m^*E_{La} - n * E_{Ni} - l^* \mu_O] / (m + n + l)$, where $E(La_mNi_nO_l)$, E_{La}, E_{Ni}, and μ_O represent the total energies of relaxed $LaNiO_3$-APB and $LaNiO_3$, pure metal La, pure metal Ni, and the chemical potential of oxygen, respectively. As a result, $LaNiO_3$-APB has a lower formation energy than $LaNiO_3$, although the value is close (Fig. 5c). It also explains that it is hard to grow films that are free of RP faults and many factors should be considered, such as formation energy, strain engineering, chemical environment and oxygen pressure, etc. In addition, the electronic structure of $LaNiO_3$-APB was also analyzed. As shown in Fig. 5d, the results of densities of state (DOS) near the interface indicate that the $LaNiO_3$-APB remains metallic properties with nonzero DOS values at the Fermi level. It should be noted that the DOS values at 1.4 Å and 5.1 Å from the interface (mainly LaO layer) are smaller than those of $NiO_{1.5}$ and NiO_2 layers at the fermi level, which echoes with the dDPC contrast analysis of the total charge intensity.

Considering the calculation and our experiments, the relaxed model with $NiO_{1.5}$-(LaO-LaO)-$NiO_{1.5}$ configuration is closed to the experiment observation of NiO_{2-x}-(LaO_y-LaO_y)-NiO_{2-x}, where the oxygen fluctuation in LaO layer is not obvious. Considering that the contrast decreases in Fig. 3b, the normalized intensity of oxygen columns in NiO_{2-x} layer is lower than 50% of that in normal NiO_2 layers. Therefore, we deduce that the configuration of the $LaNiO_3$ RP faults can be refined as: NiO_{2-x}-(LaO-LaO)-NiO_{2-x} ($0 < x < 0.5$).

4. Conclusions

In conclusion, we have investigated the atomic structure, chemical distribution, and electronic structure of the typical RP faults in a perovskite $LaNiO_3$ phase of the $LaNiO_3$ pure film and $LaNiO_3$-NiO heterostructures systematically by high-resolution STEM. HAADF- and DPC- STEM imaging technologies combined with atomic EDS mapping demonstrated that extra LaO layers stacked at the RP faults forming a NiO_{2-x}-(LaO-LaO)-NiO_{2-x} configuration ($0 < x < 0.5$). The content fluctuations of oxygen atoms and total charge density variations were also demonstrated at the RP faults. The results of line-scan EELS along the RP faults and DFT+U calculations illustrate that Ni cations have mixed valence of Ni^{2+}, Ni^{3+} at the RP faults accompanying with oxygen environment fluctuations affected by the nonstoichiometric bonding. This work offers a precise route to explore atomic chemical and physical information especially in epitaxial homointerface structures.

CRediT authorship contribution statement

Yuanmin Zhu: Writing – original draft, TEM, data analysis, Methodology, Conceptualization. **Wandong Xing:** Writing – original draft, DFT calculations, data analysis. **Ping Liao and Jiayu Liu:** TEM sample preparations, text editing, data analysis. **Jizhe Cui:** DPC-STEM data

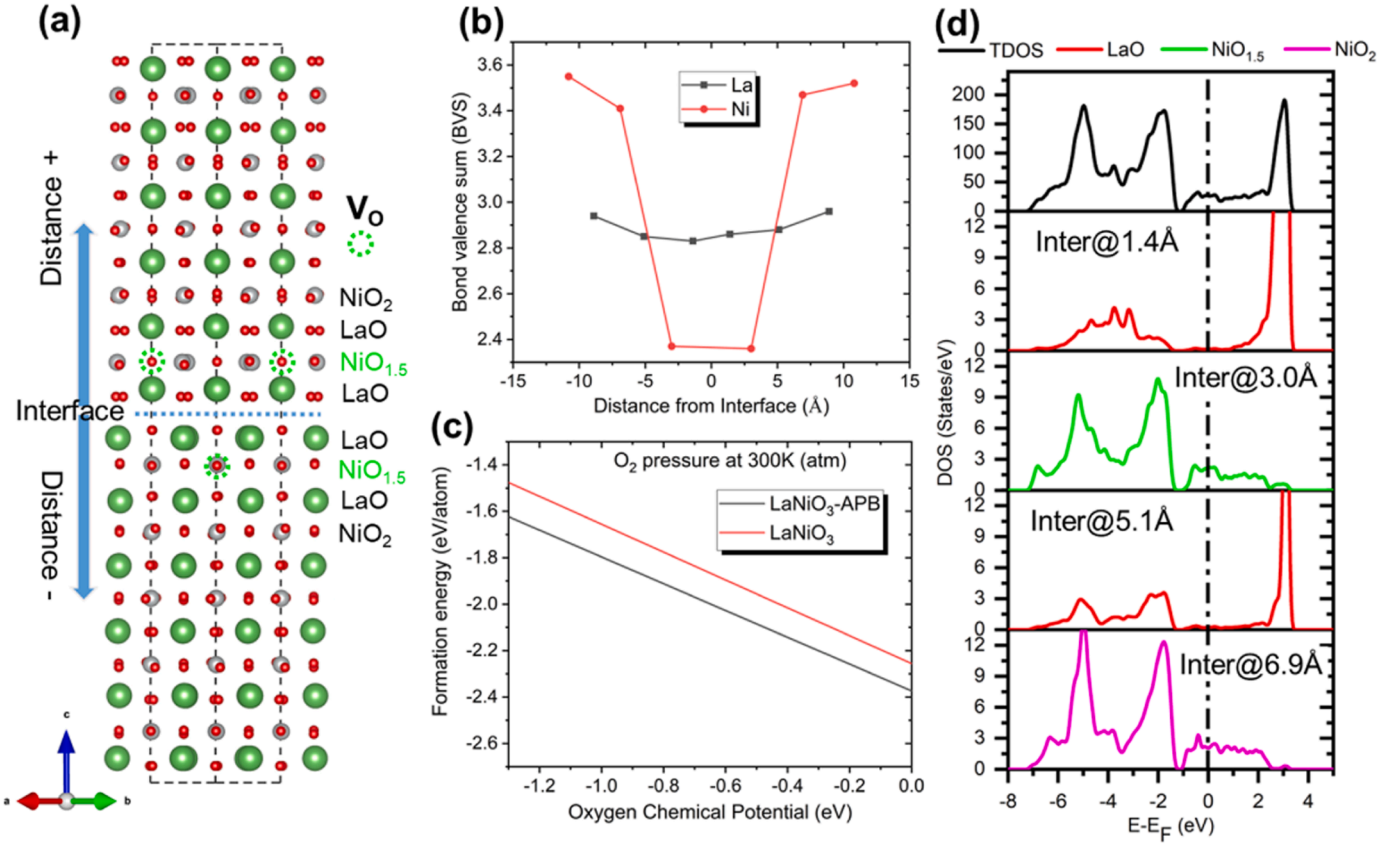

Fig. 5. (a) Atomic model of the relaxed $LaNiO_3$-APB. The structure was drawn using the VESTA program [37]. (b) BVS values of the La and Ni ions near the interface. (c) The formation energies of $LaNiO_3$-APB and $LaNiO_3$. (d) The DOS near the interface of $LaNiO_3$-APB.

analysis. **Cai Jin and Lang Chen:** PLD films growth. **Biao Wang:** Data analysis, Supervision. **Rong Yu:** TEM data analysis and discussion. All authors have read and edited the manuscript.

Declaration of Competing Interest

The authors declare that they have no known competing financial interests or personal relationships that could have appeared to influence the work reported in this paper.

Data availability

Data will be made available on request.

Acknowledgments

This work is supported by the National Natural Science Foundation of China with Grant Nos. 12004156 and 52201006, Basic and Applied Research Foundation of Guangdong Province (2022A1515140092), and (2023A1515011166). Thanks Prof. Ying-Hao Chu for providing partial film samples from National Yang Ming Chiao Tung University. The TEM work used the resources of the Electron Microscopy Center Beijing from Tsinghua University, Analyses and Testing Center from Dongguan University of Technology and Pico Center from SUSTech Core Research Facilities.

Appendix A. Supporting information

Supplementary data associated with this article can be found in the online version at doi:10.1016/j.jallcom.2023.172375.

References

[1] J.C. Yang, Q. He, Y.M. Zhu, J.C. Lin, H.J. Liu, Y.H. Hsieh, P.C. Wu, Y.L. Chen, S. F. Lee, Y.Y. Chin, H.J. Lin, C.T. Chen, Q. Zhan, E. Arenholz, Y.H. Chu, Magnetic mesocrystal-assisted magnetoresistance in manganite, Nano Lett. 14 (2014) 6073–6079, https://doi.org/10.1021/nl5019172.

[2] M. Ye, S. Hu, Y. Zhu, Y. Zhang, S. Ke, L. Xie, Y. Zhang, S. Hu, D. Zhang, Z. Luo, M. Gu, J. He, P. Zhang, W. Zhang, L. Chen, Electric polarization switching on an atomically thin metallic oxide, Nano Lett. 21 (2021) 144–150, https://doi.org/10.1021/acs.nanolett.0c03417.

[3] Y. Zhu, L. Liu, G. Cao, W. Xing, Y.H. Chu, J. Zhu, R. Yu, Atomic structure and properties of a perovskite/spinel (111) interface, Phys. Rev. B 102 (2020), 165302, https://doi.org/10.1103/PhysRevB.102.165302.

[4] K. Song, S. Ryu, H. Lee, T.R. Paudel, C.T. Koch, B. Park, J.K. Lee, S.Y. Choi, Y. M. Kim, J.C. Kim, H.Y. Jeong, M.S. Rzchowski, E.Y. Tsymbal, C.B. Eom, S.H. Oh, Direct imaging of the electron liquid at oxide interfaces, Nat. Nanotechnol. 13 (2018) 198–203, https://doi.org/10.1038/s41565-017-0040-8.

[5] Z. Wang, X. Chen, K. Huang, Y. Zhang, B. Xie, P. Yu, High-quality patterning technique for polarization-enhanced (Ba0.67Sr0.33TiO3/LaNiO3)n multi-interface multilayer hetero-structure, J. Alloy. Compd. 788 (2019) 712–718, https://doi.org/10.1016/j.jallcom.2019.02.248.

[6] T. Hibma, F.C. Voogt, L. Niesen, P.A.A. van der Heijden, W.J.M. de Jonge, J.J.T. M. Donkers, P.J. van der Zaag, Anti-phase domains and magnetism in epitaxial magnetite layers, J. Appl. Phys. 85 (1999) 5291, https://doi.org/10.1063/1.369857.

[7] Y. Guo, B. Liu, W. Xie, Q. Luo, Q. Li, Anti-phase boundary energy of β series precipitates in Mg-Y-Nd system, Scr. Mater. 193 (2021) 127–131, https://doi.org/10.1016/j.scriptamat.2020.11.004.

[8] X.-K. Wei, A.K. Tagantsev, A. Kvasov, K. Roleder, C.-L. Jia, N. Setter, Ferroelectric translational antiphase boundaries in nonpolar materials, Nat. Commun. 5 (2014) 3031, https://doi.org/10.1038/ncomms4031.

[9] S. Ahmed, A. Pokle, M. Bianchini, S. Schweidler, A. Beyer, T. Brezesinski, J. Janek, K. Volz, Understanding the formation of antiphase boundaries in layered oxide cathode materials and their evolution upon electrochemical cycling, Matter 4 (2021) 3953–3966.

[10] Z. Wang, H. Guo, S. Shao, M. Saghayezhian, J. Li, R. Fittipaldi, A. Vecchione, P. Siwakoti, Y. Zhu, J. Zhang, Designing antiphase boundaries by atomic control of heterointerfaces, Proc. Natl. Acad. Sci. 115 (2018) 9485–9490.

[11] T. Heisig, J. Kler, H. Du, C. Baeumer, F. Hensling, M. Glöß, M. Moors, A. Locatelli, T.O. Menteş, F. Genuzio, Antiphase boundaries constitute fast cation diffusion paths in SrTiO3 memristive devices, Adv. Funct. Mater. 30 (2020) 2004118.

[12] T. Hungría, J.G. Lisoni, A. Castro, Sr3Ti2O7 Ruddlesden−Popper phase synthesis by milling routes, Chem. Mater. 14 (2002) 1747–1754, https://doi.org/10.1021/CM0115012.
[13] K.M. Satyalakshmi, R.M. Mallya, K. v Ramanathan, X.D. Wu, B. Brainard, D. C. Gautier, N.Y. Vasanthacharya, M.S. Hegde, Epitaxial metallic LaNiO3 thin films grown by pulsed laser deposition, Appl. Phys. Lett. 62 (1998) 1233, https://doi.org/10.1063/1.109612.
[14] J. Fowlie, M. Gibert, G. Tieri, A. Gloter, J. Íñiguez, A. Filippetti, S. Catalano, S. Gariglio, A. Schober, M. Guennou, J. Kreisel, O. Stéphan, J.-M.J. Triscone Fowlie, M. Gibert, G. Tieri, S. Catalano, S. Gariglio, J. Triscone, A. Gloter, O. Stéphan, J. Íñiguez, A. Schober, M. Guennou, J. Kreisel, A. Filippetti, Conductivity and local structure of LaNiO3 thin films, Adv. Mater. 29 (2017) 1605197, https://doi.org/10.1002/ADMA.201605197.
[15] S.N. Ruddlesden, P. Popper, The compound Sr3Ti2O7 and its structure, Acta Crystallogr. 11 (1958) 54–55.
[16] J. Bak, S.Y. Chung, Observation of fault-free coherent layer during Ruddlesden–Popper faults generation in LaNiO3 thin films, J. Korean Ceram. Soc. 58 (2021) 169–177, https://doi.org/10.1007/S43207-020-00080-7/FIGURES/5.
[17] R.G. Palgrave, P. Borisov, M.S. Dyer, S.R.C. McMitchell, G.R. Darling, J.B. Claridge, M. Batuk, H. Tan, H. Tian, J. Verbeeck, J. Hadermann, M.J. Rosseinsky, Artificial construction of the layered Ruddlesden–Popper manganite La2Sr2Mn3O10 by reflection high energy electron diffraction monitored pulsed laser deposition, J. Am. Chem. Soc. 134 (2012) 7700–7714, https://doi.org/10.1021/ja211138x.
[18] M. Fujimoto, T. Suzuki, Y. Nishi, K. Arai, J. Tanaka, Calcium-ion selective site occupation at Ruddlesden-Popper-type faults and the resultant dielectric properties of a-site-excess strontium calcium titanate ceramics, J. Am. Ceram. Soc. 81 (1998) 33–40.
[19] T. Nakamura, R. Oike, Y. Ling, Y. Tamenori, K. Amezawa, The determining factor for interstitial oxygen formation in Ruddlesden–Popper type La2NiO4-based oxides, Phys. Chem. Chem. Phys. 18 (2016) 1564–1569.
[20] K.M. Satyalakshmi, R.M. Mallya, K.V. Ramanathan, X.D. Wu, B. Brainard, D. C. Gautier, N.Y. Vasanthacharya, M.S. Hegde, Epitaxial metallic LaNiO3 thin films grown by pulsed laser deposition, Appl. Phys. Lett. 62 (1993) 1233–1235.
[21] M.C. Weber, M. Guennou, N. Dix, D. Pesquera, F. Sánchez, G. Herranz, J. Fontcuberta, L. López-Conesa, S. Estradé, F. Peiró, J. Iñiguez, J. Kreisel, Multiple strain-induced phase transitions in LaNiO3 thin films, Phys. Rev. B 94 (2016), 014118, https://doi.org/10.1103/PhysRevB.94.014118.
[22] S. Venzke, R.B. van Dover, J.M. Phillips, E.M. Gyorgy, T. Siegrist, C.-H. Chen, D. Werder, R.M. Fleming, R.J. Felder, E. Coleman, R. Opila, Epitaxial growth and magnetic behavior of NiFe2O4 thin films, J. Mater. Res. 11 (1996) 1187–1198, https://doi.org/10.1557/JMR.1996.0153.
[23] Y.M. Zhu, T.H. Do, V.T. Tra, R. Yu, Y.-H. Chu, Q. Zhan, Atomic heterointerfaces and electrical transportation properties in self-assembled LaNiO3-NiO heteroepitaxy, Adv. Mater. Interfaces 5 (2018) 1701202, https://doi.org/10.1002/admi.201701202.
[24] C. Jin, Y. Zhu, X. Li, F. An, W. Han, Q. Liu, S. Hu, Y. Ji, Z. Xu, S. Hu, M. Ye, G. Zhong, M. Gu, L. Chen, Super-flexible freestanding BiMnO3 membranes with stable ferroelectricity and ferromagnetism, Adv. Sci. 8 (2021) 2102178, https://doi.org/10.1002/ADVS.202102178.
[25] P.E. Blöchl, Projector augmented-wave method, Phys. Rev. B 50 (1994) 17953, https://doi.org/10.1103/PhysRevB.50.17953.
[26] G. Kresse, J. Furthmüller, Efficient iterative schemes for ab initio total-energy calculations using a plane-wave basis set, Phys. Rev. B 54 (1996) 11169, https://doi.org/10.1103/PhysRevB.54.11169.
[27] W. Xing, H. Sha, F. Meng, R. Yu, Stabilization of the (1 1 1) surface of NiO and CoO by segregation of point defects, Appl. Surf. Sci. 582 (2022), 152473.
[28] W. Xing, R. Yu, Atomic structures of high Miller index surfaces of NiO, J. Mater. Chem. C Mater. 8 (2020) 14164–14171, https://doi.org/10.1039/D0TC04043F.
[29] W. Xing, Y. Zhang, J. Zhu, R. Yu, Structural and spin state transition in the polar NiO(111) surface, Appl. Surf. Sci. 532 (2020), 147427, https://doi.org/10.1016/j.apsusc.2020.147427.
[30] H.J. Monkhorst, J.D. Pack, Special points for Brillouin-zone integrations, Phys. Rev. B 13 (1976) 5188–5192, https://doi.org/10.1103/PhysRevB.13.5188.
[31] I.D. Brown, The Chemical Bond in Inorganic Chemistry: the Bond Valence Model, Oxford University Press, 2016.
[32] I. Lazić, E.G.T. Bosch, S. Lazar, Phase contrast STEM for thin samples: Integrated differential phase contrast, Ultramicroscopy 160 (2016) 265–280, https://doi.org/10.1016/j.ultramic.2015.10.011.
[33] S. Fang, Y. Wen, C.S. Allen, C. Ophus, G.G.D. Han, A.I. Kirkland, E. Kaxiras, J. H. Warner, Atomic electrostatic maps of 1D channels in 2D semiconductors using 4D scanning transmission electron microscopy, Nat. Commun. 10 (2019), https://doi.org/10.1038/s41467-019-08904-9.
[34] W. Wang, J. Cui, Z. Sun, L. Xie, X. Mu, L. Huang, J. He, Direct atomic-scale structure and electric field imaging of triazine-based crystalline carbon nitride, Adv. Mater. 33 (2021), https://doi.org/10.1002/adma.202106359.
[35] G. Sánchez-Santolino, N.R. Lugg, T. Seki, R. Ishikawa, S.D. Findlay, Y. Kohno, Y. Kanitani, S. Tanaka, S. Tomiya, Y. Ikuhara, N. Shibata, Probing the internal atomic charge density distributions in real space, ACS Nano 12 (2018) 8875–8881, https://doi.org/10.1021/acsnano.8b03712.
[36] K. Xu, T. Lin, Y. Rao, Z. Wang, Q. Yang, H. Zhang, J. Zhu, Direct investigation of the atomic structure and decreased magnetism of antiphase boundaries in garnet, Nat. Commun 13 (2022) 1–10, https://doi.org/10.1038/s41467-022-30992-3.
[37] K. Momma, F. Izumi, *VESTA3* for three-dimensional visualization of crystal, volumetric and morphology data, J. Appl. Crystallogr. 44 (2011) 1272–1276, https://doi.org/10.1107/S0021889811038970.